Optimize An MRI Gauss Gun

A Thesis
Presented to
the Faculty of the Department of Electrical and Computer Engineering
University of Houston

in Partial Fulfillment
of the Requirements for the Degree
Master of Science
in Electrical Engineering

by
Mohammad M. Sultan
December 2017

Optimize An MRI Gauss Gun

Mohammad M. Sultan

Approved:

Chairman of the Committee
Aaron T. Becker, Assistant Professor
Department of Electrical and Computer Engineering

Committee Members:

Jack Wolfe, Professor
Department of Electrical and Computer Engineering

Jose Luis Contreras-Vidal, Professor
Department of Electrical and Computer Engineering

Nikolaos Tsekos, Associate Professor
Department of Computer Science

Suresh K. Khator, Associate Dean
Cullen College of Engineering

Badrinath Roysam, Professor Chair
Electrical and Computer Engineering

Acknowledgment

First, I express my utmost appreciation to Dr. Aaron T. Becker for his unwavering support and guidance throughout this journey. I would also like to mention that Dr. Becker is the driving force behind my decision to switch to the thesis path in the robotics field, as I was inspired by him after taking his robotics class. I want to thank Dr. Julien Leclerc, post-doctoral researcher at the Robotic Swarm Control Lab, for his valuable assistance in the FEMM software. A large thank you is due for Jarret Lonsford and Javier Garcia for their help in the experiments, and to everyone at the *Robotic Swarm Control Lab* for always providing me with their assistance when it was needed. Last but not least, my deepest gratitude goes to my parents, siblings and fiancée Tasneem for their constant encouragement and support in my attainment of this goal.

Optimize An MRI Gauss Gun

An Abstract

of a

Thesis

Presented to

the Faculty of the Department of Electrical and Computer Engineering

University of Houston

in Partial Fulfillment

of the Requirements for the Degree

Master of Science

in Electrical and Computer Engineering

by

Mohammad M. Sultan

December 2017

Abstract

MRI-based navigation and propulsion of millirobots is a new and promising approach for minimally invasive therapies. The strong constant magnetic field inside the scanner precludes torque-based control. Consequently, prior propulsion techniques have been limited to gradient-based pulling through fluid-filled body lumens using the weaker gradient magnetic coils. Performing interventions requires techniques or mechanism to increase this weak magnetic pulling force. One technique is a self-assembling robotic tool designed by our lab called a *Gauss gun*. This thesis shows numerical analysis and results for optimizing the kinetic energy generated by a Gauss gun to penetrate tissue, deliver a drug or remove a clot. This analysis based on the equations of energy for an MRI Gauss gun. The numerical method used for this optimization is Nelder Mead, implemented in *Mathematica* software.

Table of Contents

Acknowledgment ..... **iv**

Abstract ..... **vi**

Table of Contents ..... **vii**

List of Figures ..... **ix**

List of Tables ..... **xii**

List of Samples ..... **xiii**

Chapter 1 ..... **1**

Chapter 2 ..... **7**

2.1 Penetration Tests 8

2.2 Self-Assembly Tests 8

2.3 Auto-Injectors 9

2.3.1 Design 10

2.3.2 MRI Gauss Gun and Auto-Injector comparison 11

2.4 An MRI Gauss Gun Vs. Spring 11

MRI Gauss Gun Force, Torque, Design, Materials and Energy System **13**

3.1 Magnet Force Calculation inside MRI 13

3.2 Magnetic Torque on MRI Gauss Gun 15

3.3 MRI Gauss Gun Design 16

3.4 MRI Gauss Gun Materials 17

3.5 MRI Gauss Gun Magnetic Energy to Kinetic Energy 18

3.5.1 Kinetic and Potential Energies in MRI Gauss Gun System 18

3.5.2 Numerical and Analytical Methods using Mathematica 20

MRI Gauss Gun Optimization – Analytical and Numerical Results 23

4.1 MRI Gauss Gun Restrictions 23

4.2 Analytical and Results 24

4.2.1 Numerical and Analytical Methods using Mathematica 24

4.2.2 Numerical Analysis when all millirobots have the same radii 26

4.2.3 Numerical Analysis using different radii when $N = 1$ and $N = 2$ 30

4.3 Study Cases 33

4.3.1 Study Case 1: Designing MRI Gauss Gun for brachytherapy delivery in the bladder (limited radius size to insert each component, very large area to assemble). 33

4.3.2 Study Case 2: Designing MRI Gauss Gun for *cyst fenestration* in brain ventricle, entry through the spinal canal. 35

4.3.3 Study Case 3: Designing MRI Gauss Gun for clot removal case from the coronary artery. 39

Conclusion 42

References 44

List of Figures

Figure 1.1 Operation of a Gauss Gun. (a) Standard design for use outside an MRI scanner shown before and after triggering. Magnetized spheres are green. Non-magnetized spheres are gray. (b) Design for use inside an MRI scanner shown before and after triggering. All spheres are magnetized when inside the scanner. See video at http://youtu.be/uJ4rFA8x2Js. 3

Figure 1.2 Schematic of a brachytherapy seed. These are used to treat prostate cancer. 4

Figure 1.3 Fluid-filled spaces in the brain ventricle have dimensions suitable for an MRI Gauss Gun to deliver a drug to help removing brain tumor. Image credit: 4

Figure 1. 4 An MRI Gauss gun has dimensions that could be sized to remove a heart attack-causing clot from the coronary artery. Image credit: https://www.nhlbi.nih.gov/health/health-topics/topics/heartattack. 5

Figure 1. 5 Shows the bladder and the urinary system . Image credit: https://medical-dictionary.thefreedictionary.com/bladder. 5

Figure 2.1 (a) MRI Gauss Gun components. (b) Cross-section, three components MRI Gauss Gun before and after firing. 7

Figure 2.2 Photos from an experiment within the MRI bore. The membrane model is a water balloon filled with dye. See the video attachment. T = Trigger D = Delivery B = Barrel. 9

Figure 2.3 Auto-Injector. Image credit: http://www.sumainject.com/aspx/HowToUse.aspx. 10

Figure 2.4 Auto Injector cross section. Image credit: https://www.picoauto.com/library/automotive-guided-tests/multi-point-current/..... 10
Figure 2.5 Spring Image credit: http://www.efunda.com/designstandards/springs/calc_comp_designer.cfm. 11
Figure 3. 1 Contour lines show the force component radially outward from a sphere at (0,0) on an identical sphere in an MRI. The magnetic field is symmetric about the z-axis. 14
Figure 3.2 Three stages MRI Gauss Gun with all the components, (a) Trigger component, (b) Barrel component contains two stages and (c) Delivery component. 17
Figure 3.3 One stage MRI Gauss Gun contains only of (a) trigger component and (c) delivery component with no barrel component. 17
Figure 3.4 shows how the energy system works in three stage MRI Gauss Gun (a) the trigger component is moving with $+KE\infty$_ini to the first stage from the MRI Gauss Gun, (b) trigger component hits first sphere with energy equals to $+KE\infty$, (c) sphere 3 hits sphere 4 with energy equals to $+KE\infty - PEMB + KEa$, (d) sphere 5 hits sphere 6 with energy equals to $+KE\infty - 2PEMB + 2KEa$and (e) the delivery part moves with energy $+KE\infty - 3PEMB + 2KEa$. 22
Figure 4. 1 Three stage MRI Gauss Gun. 23
Figure 4.2 kineticEnergy[r,N] function created in Mathematica to be used in MRI Gauss Gun optimization. 26
Figure 4. 3 plot $\boldsymbol{KE/L3}$ Vs $\boldsymbol{r/L}$ for $\boldsymbol{N}$ from 1 to 10. Each curve represents a stage. The red dots represent the optimum value for each stage. 27
Figure 4.4 Different stage MRI Gauss Gun with the same length $\boldsymbol{L}$ 28

Figure 4. 5 (a) Contour Plot for $\boldsymbol{r1/L}$ Vs $\boldsymbol{r2/L}$, (b) Contour Plot for $\boldsymbol{s/L}$ Vs $\boldsymbol{r3/L}$. 30

Figure 4.6 Shows different one stage MRI Gauss Gun that represent the red points in Figure 4.5 31

Figure 4.7 (a) one stage optimum MRI Gauss Gun with different radii case and (b) two stages optimum MRI Gauss Gun with different radii case. 33

Figure 4.8 Mathematica code to find the optimum value for a,s and N to optimize KE inside the bladder 34

Figure 4. 9 Optimized MRI Gauss Gun to fit inside the bladder 34

Figure 4.10 Schematic showing an MRI Gauss Gun inside a bladder..... 35

Figure 4. 11 Mathematica code to find the optimum value for a,s and N to optimize KE inside male brain ventricle 37

Figure 4.12 Schematic showing an MRI Gauss Gun inside male brain ventricle 37

Figure 4. 13 Mathematica code to find the optimum value for a,s and N to optimize KE inside female brain ventricle 38

Figure 4.14 Schematic showing an MRI Gauss Gun inside female brain ventricle 38

Figure 4.15 Mathematica code to find the optimum value for $\boldsymbol{a, s}$ and $\boldsymbol{N}$ to optimize $\boldsymbol{KE}$... 39

Figure 4.16 Groin area. Image credit: https://www.epainassist.com/pelvic-pain/groin-pain..... 40

Figure 4.17 Aorta Anatomy. Image credit: http://www.jems.com/articles/print/volume-41/issue-3/features/how-aortic-aneurysms-become-aortic-catastrophes.html..... 40

Figure 4.18 Schematic showing an MRI Gauss Gun inside coronary artery..... 41

List of Tables

4.1 represents the optimum value in each stage from N = 1 to 10..... 29

4.2 The optimal values for a single unit Gauss gun, shown as red points in Figure 4.4..... 32

4.3 Shows the optimum values for r, r1, r2, r3, r4, s, a and KE when L=1. 32

4.4 CT scan measurements (mean ±standard deviation) of frontal horn of lateral ventricle. https://www.researchgate.net/publication/268449358_Age-related_changes_in_ventricular_system_of_brain_in_normal_individuals_by_computed_tomography_scans..... 36

List of Samples

$\boldsymbol{a}$: air gap.

d: is the distance separating the two spheres with radii's r_1 and r_2.

$\boldsymbol{KE_{\infty}}$**:** is the kinetic energy that the fired millirobot gains by the attraction force causes from the first millirobot when it getting close to it in the first stage.

$\boldsymbol{KE_a}$**:** is the kinetic Energy that the millirobot gains by the attraction force causes from the first millirobot in the next stage when it moves a distance from current stage to the next stage.

$\boldsymbol{KE_f}$**:** final Kinetic energy.

$\boldsymbol{L}$: MRI Gauss Gun Length.

MRI: Magnetic Resonance Imaging.

$\boldsymbol{M_s}$**:** is the magnetic saturation inside MRI = $1.36 \cdot 10^6$.

$\boldsymbol{N}$: total barrel and delivery components.

$\boldsymbol{PE_{MB}}$: is the potential energy between any two millirobots inside each stage before firing.

$\boldsymbol{r}$: millirobot radius.

$\boldsymbol{s}$: non-magnetic spacer.

$\boldsymbol{\tau}$: the torque

$\boldsymbol{\mu_o}$: vacuum permeability which is equal to $4\pi \cdot 10^{-7}$ V.s/(A.m).

Chapter 1

Introduction

A useful categorization of small-scale robots is to classify them by their largest dimension as millirobots, microrobots, or nanorobots. *Millirobots* are robots having dimensions typically less than a centimeter [1], *microrobots* are robots with dimensions less than 1 mm, and *nanorobots* are robots whose components are at or near the scale of a nanometer. In this thesis, we are interested in millirobots and their applications

Millirobots have the potential to provide highly localized therapies with minimal trauma by navigating through the natural fluid-filled passageways of the body. While navigation, e.g., the circulatory system or cerebrospinal fluid spaces, is sufficient for some applications, it can also be necessary to penetrate into the surrounding tissue. Potential applications include puncturing a membrane to release trapped fluid, opening a blocked passageway, delivering a drug to a tissue location several centimeters from a fluid-filled space or brachytherapy Figure 1.4 shows a brachytherapy seed which is used to treat prostate cancer by killing fast-dividing tumor cells.

The forces required for tissue penetration, however, are substantially higher than those needed to propel a millirobot through a bodily fluid and consequently can be difficult to achieve. Prior tetherless systems for moving through tissue have relied on magnetic forces and torques produced by large external magnets to either pull magnetic spheres through brain tissue [2] or to rotate threaded magnetic cylinders through muscle tissue [3].

Alternatively, methods for tetherless robot propulsion and control have been developed that employ the magnetic gradients of clinical MRI scanners [4]–[7]. MRI also provides the capability to image both the robot and surrounding tissue to guide navigation. MRI-based millirobot navigation in the vasculature was first demonstrated in [4]. Recently, algorithms enabling the simultaneous MRI-based control of multiple millirobots [5], [8] and macro-scale rotary actuators [6], [7] have also been developed.

Until now, however, the motion of MRI-powered millirobots has been constrained to fluid-filled spaces since the magnetic gradients produced by the scanner are relatively weak. The maximum gradient produced by most clinical scanners is in the range of 20-40mT/m producing a force on a magnetized steel particle equal to 36-71% of the gravitational force. While it is possible to install custom high-strength gradient coils, such as 400mT/m coil reported in [8], this approach is costly and can reduce the size of the MRI bore. While to facilitate motion within a fluid, a millirobot can be designed to be neutrally buoyant, the force magnitude produced by the magnetic gradient is not capable of producing tissue penetration.

Design can reduce the force required for penetration. Aa standard 18-gauge needle requires 0.59 ± 0.11N of force to penetrate 10mm into muscle tissue [10]. Bioinspired design can somewhat reduce these forces, e.g., the backward-tipped barbs of the North American porcupine quill exhibit forces of 0.33 ± 0.08N for 10mm of muscle penetration [10]. Nevertheless, to reproduce even these forces using an MRI with a steel needle would require 3.3m long shaft – longer than the bore of the scanner. While the size of macro-scale MRI-based actuators permits the use of gear transmissions to trade off velocity and force [5], [11], this approach is not feasible at the millimeter scale.

Therefore, to address the challenge of MRI-based tissue penetration, an alternative to gradient – based force production is needed.

The concept, illustrated in Figure 1.2, corresponds to a Gauss Gun [13],[14]. Comprised of one or more stages, each stage is composed of a strong magnet, followed by two or more steel spheres (bearing balls). By colliding a single steel sphere with the first magnet, a chain reaction is initiated, greatly amplifying the speed of the first sphere.

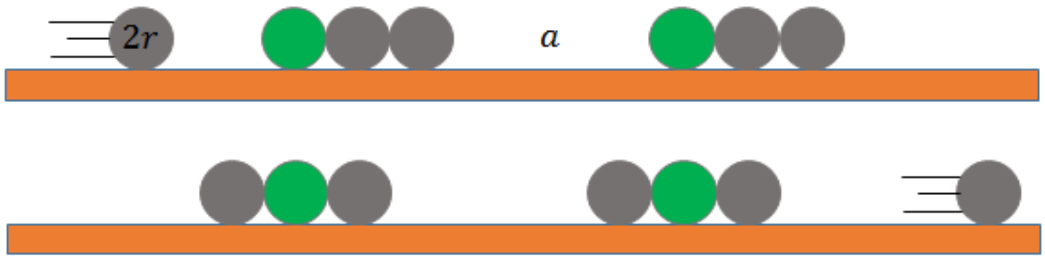

(a) Traditional Gauss Gun before and after triggering

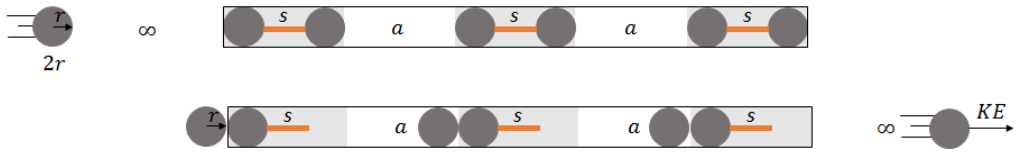

(b) MRI Gauss Gun before and after triggering

Figure 1.1 Operation of a Gauss Gun. (a) Standard design for use outside an MRI scanner shown before and after triggering. Magnetized spheres are green. Non-magnetized spheres are gray. (b) Design for use inside an MRI scanner shown before and after triggering. All spheres are magnetized when inside the scanner. See video at http://youtu.be/uJ4rFA8x2Js.

In an MRI scanner there is no need for permanent magnets, since steel is highly magnetized by 3T magnetic field of an MRI. Each stage contains two magnetized spheres separated by a nonmagnetic spacer, in individually stable. Using existing control approaches [5], [7], they can be navigated through fluid-filled spaces and self-assembled

at a desired penetration location. The assembly can then be fired by a special trigger module consisting of two spheres separated by a spacer longer than that used in the individual stages. After firing, the assembly can be navigated out of the body. Figure 1.2, Figure 1.3, Figure 1.4 and 1.5 show places in the human anatomy that have potential for application of an MRI Gauss Gun

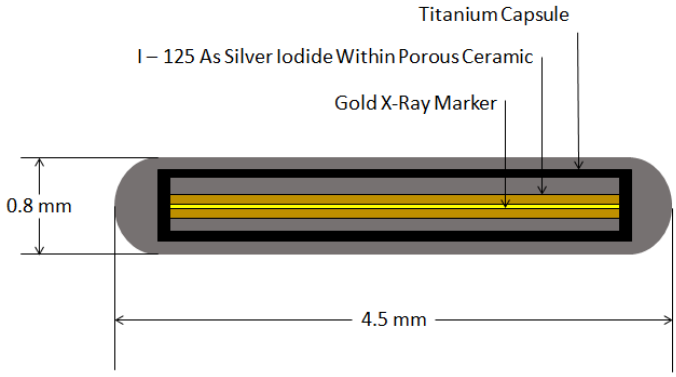

Figure 1.2 Schematic of a brachytherapy seed. These are used to treat prostate cancer.

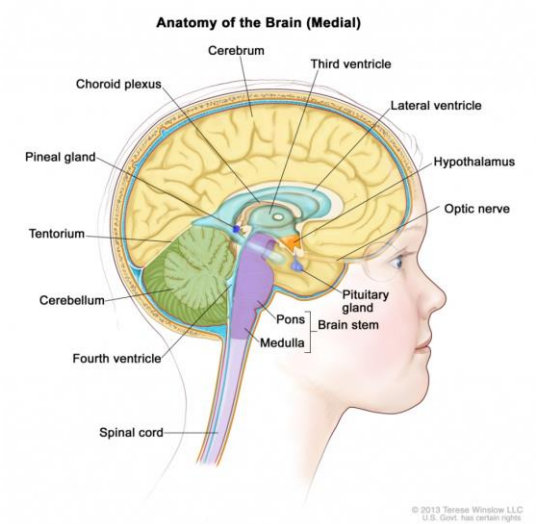

Figure 1.3 Fluid-filled spaces in the brain ventricle have dimensions suitable for an MRI Gauss Gun to deliver a drug to help removing brain tumor. Image credit: http://humananatomylibrary.com/anatomy-of-the-lateral-ventricle/anatomy-of-the-lateral-ventricle-anatomy-of-brain-ventricles-hu.

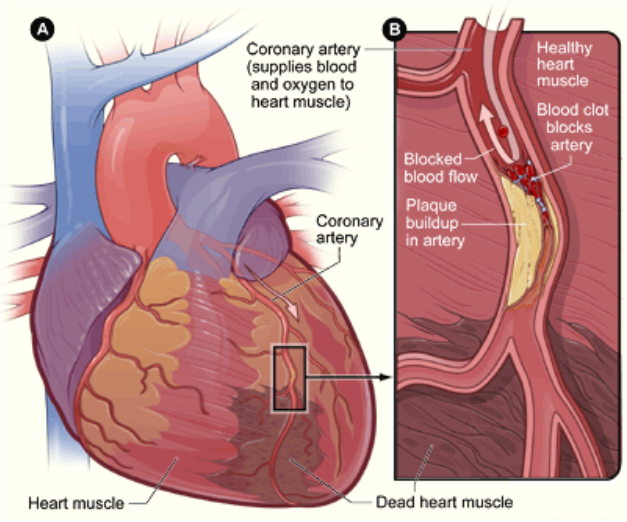

Figure 1. 4 **An MRI Gauss gun has dimensions that could be sized to remove a heart attack-causing clot from the coronary artery. Image credit: https://www.nhlbi.nih.gov/health/health-topics/topics/heartattack.**

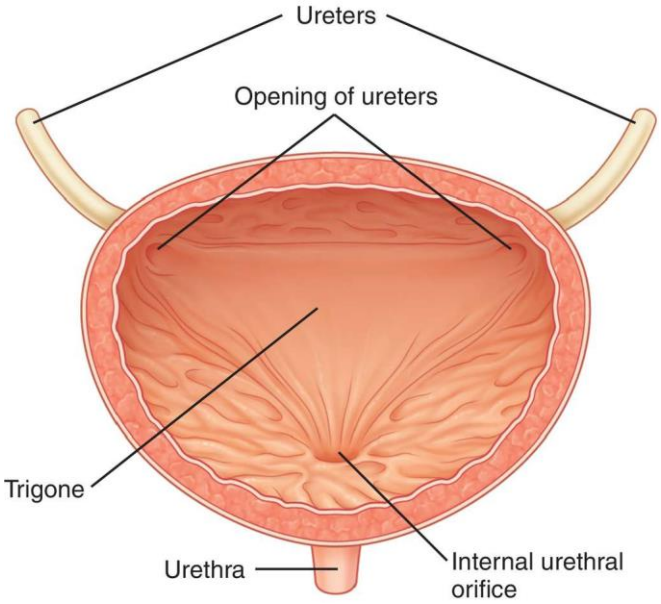

Figure 1.5 **Shows the bladder and the urinary system . Image credit: https://medicaldictionary.thefreedictionary.com/bladder**

The next chapter shows related work done using a clinical MRI. The third chapter explains the force, the torque and the energy inside MRI Gauss Gun also the design and

the material used for design. Chapter four discusses numerical, analytical and study cases for the MRI Gauss Gun. The last chapter is the conclusion of this work and possible future work.

Chapter 2

Related Work

The MRI Gauss Gun components as in Figure 2.1 were tested in a Siemen's Skyra 3T clinical MRI scanner. Experiments tested penetration depth as a function of needle size and the ability of components to self-assemble. These results are from the paper *Toward Tissue Penetration by MRI-powered Millirobots Using a Self-Assembled Gauss Gun*.

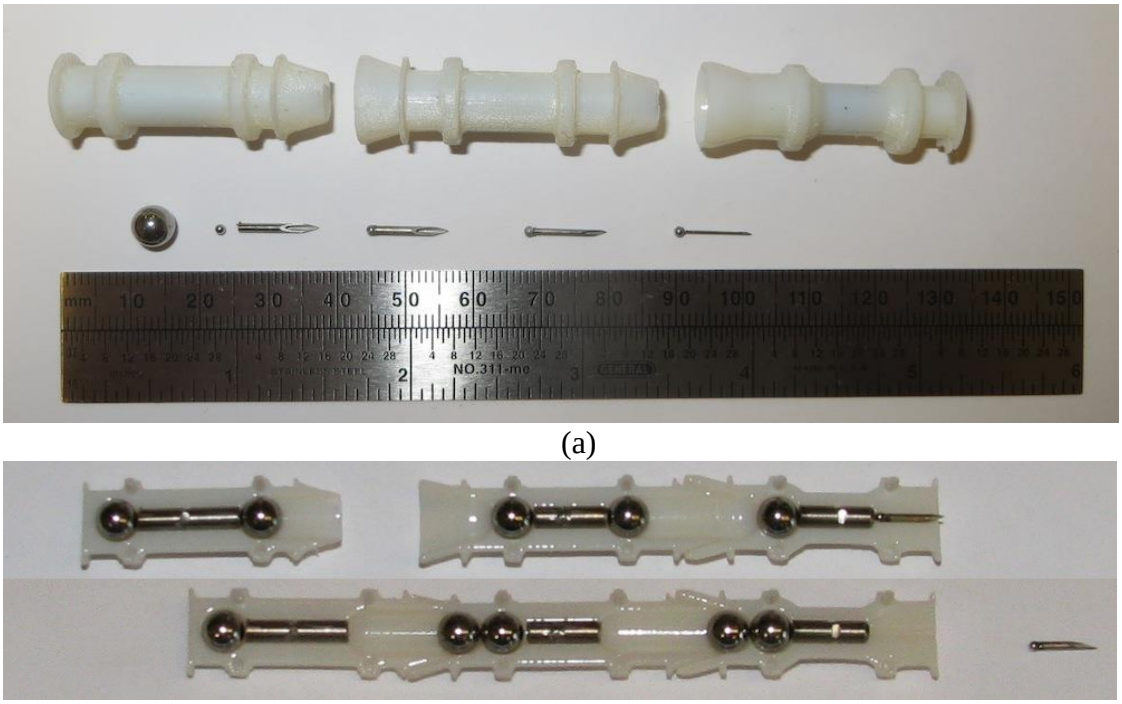

(a)

(b)

Figure 2.1 (a) MRI Gauss Gun components. (b) Cross-section, three components MRI Gauss Gun before and after firing.

2.1 Penetration Tests

Several experiments were conducted to test the ability of the MRI-Gauss gun at tissue penetration. The tests use a brain model composed of a solidified 0.5% agarose gel solution [19]. A 30mm block of agarose was used and placed near the isocenter of a Siemen's Skyra 3T MRI scanner. The delivery component, loaded with either an 18, 20, or 26-gauge needle, was placed against the solution. Zero, one or two barrel components were attached, and the trigger component was then manually pushed toward the assembled Gauss gun. Needle penetration was measured using a plastic ruler mounted underneath the transparent agar solution.

The experiments results are represented in Figure 2.2. Five trials were recorded for each needle size. The penetration distance increases as the gauge increases (needle diameter decreases).

2.2 Self-Assembly Tests

Figure 2.2 shows photos from two experiments with MRI Gauss Gun assembly and membrane penetration. The experiments were performed under MRI control, using gradients in the x and z-direction of_23mT/m. The workspace was a plastic toolbox (McMaster-Car 8704T73) filled with water. The Gauss gun components were mounted on floats and colored green to increase visibility. Three tests were performed, and are included in the video attachment. The first two experiments each used a delivery and a trigger component and fired 18-gauge needle tips welded to 1mm spheres into a membrane model, a water balloon filled with blue dye. The third experiment tested

ranged delivery, by firing the needle projectile using a delivery, barrel, and trigger component to penetrate a membrane model from a distance of 240 mm.

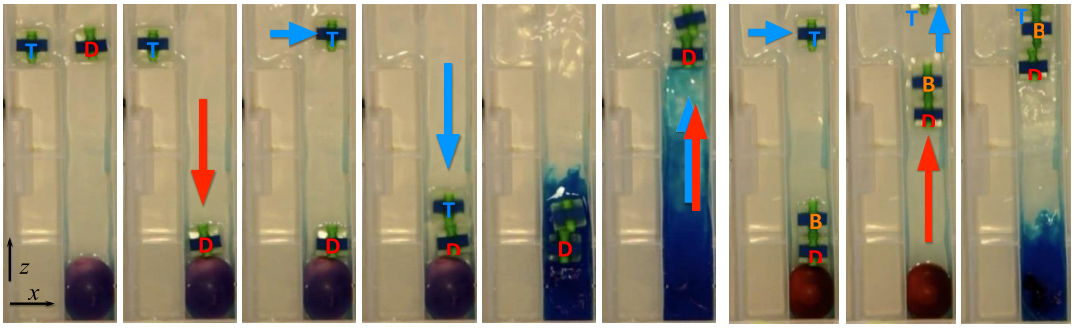

Figure 2.2 Photos from an experiment within the MRI bore. The membrane model is a water balloon filled with dye. See the video attachment. T = Trigger D = Delivery B = Barrel.

(a) Membrane puncture, two components (b) Membrane puncture three components

2.3 Auto-Injectors

An *auto-injector* is a medical device designed to deliver a dose of a particular drug. Most auto-injectors are spring-loaded syringes. By design, auto-injectors are easy to use and are intended for self-administration by patients, or administration by untrained personnel. The site of injection depends on the drug loaded, but it typically is administered into the thigh or the buttocks. The injectors were initially designed to overcome the hesitation associated with self-administration of the needle-based drug delivery device [30].

Figure 2.3 Auto-Injector. Image credit: http://www.sumainject.com/aspx/HowToUse.aspx.

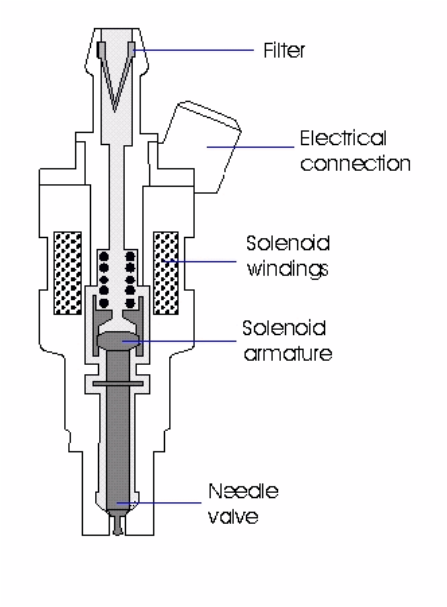

Figure 2.4 Auto Injector cross-section. Image credit: https://www.picoauto.com/library/automotive-guided-tests/multi-point-current/.

2.3.1 Design

The auto-injector keeps the needle tip shielded prior to injection and also has a passive safety mechanism to prevent accidental firing (injection). Injection depth can be adjustable or fixed and a function for needle shield removal may be incorporated. Just by pressing a button, the syringe needle is automatically inserted and the drug is delivered. Once the injection is completed some auto injectors have the visual indication to confirm that the full dose has been delivered. Auto-injectors often contain glass syringes, which

can make them fragile and contamination can occur. More recently, companies have been looking into making auto-injector syringes out of plastic to prevent this issue [30].

2.3.2 MRI Gauss Gun and Auto-Injector comparison

MRI Gauss Guns and auto-injectors can be used for drug delivery with two main differences, the needs for MRI and the energy source. MRI Gauss Gun needs the MRI to work while the auto-injector does not need it. The MRI Gauss Gun energy source is the Gauss Gun while the auto-injector energy source is the spring.

2.4 An MRI Gauss Gun Vs. Spring

Spring is an elastic object that stores mechanical energy. Springs are often made of spring steel. This section will show the difference between the energy released by the MRI Gauss Gun and the spring.

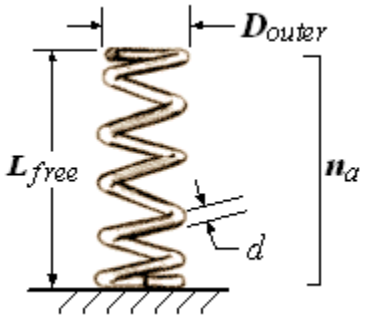

Figure 2. 5 Spring schematic. Image credit: http://www.efunda.com/designstandards/springs/calc_comp_designer.cfm.

For an ideal linear spring, the kinetic energy equations are:

$$KE_{\text{spring}} = \frac{1}{2} k x^2, \tag{2.1}$$

$$k = \frac{Gd^4}{8D^3 n_a}, \tag{2.2}$$

$G = \frac{E}{2(1+v)}$, and (2.3)

$D = D_{outer} - d.$ (2.4)

- KE_{spring}: spring kinetic energy
- k: spring constant
- x: spring distance
- E: elastic modules
- v: Poisson ratio
- D: mean diameter of the spring
- d: spring thickness

For our spring we will use $L_{free} = 10$ mm, $D_{outer} = 2r = 2$ mm, $n_a = \frac{L_{free} - 2r}{d}$, d = 4 mm, and composed of Nickel titanium which has elastic modulus = 75 – 83 and a Poisson ratio of 0.33 [35].

These equations generate $k = 4300$ N/m and $\boldsymbol{KE_{spring}}$ **= 0.0086 J**

Using the same scale for the MRI Gauss Gun with L = 10 mm and r = 1 mm, using *Mathematica* (this code will be covered on chapters 4), N = 1, s = 4 mm

KE = 0.007 J.

While the spring has more energy, the key advantage for the MRI Gauss Gun is that it can be assembled inside the body while the spring cannot.

Chapter 3

MRI Gauss Gun Force, Torque, Design, Materials and Energy System

3.1 Magnet Force Calculation inside MRI

Ferrous material placed inside the MRI scanner becomes a strong magnetic dipole. The gradient fields can then apply forces on these dipoles. The dipoles exert forces on each other.

The magnetic field at position p_2 generated by a spherical magnet at position p_1 with magnetic moment m_1 is

$$B_{p_1}(p_2) = \frac{3\mu_o}{4\pi} \frac{3n_{12}(n_{12}.m_1) - m_1}{|p_2 - p_1|^3} \ , \tag{3.1}$$

while $n_{12} = \frac{p_2 - p_1}{|p_2 - p_1|}$ This is the magnetic field of a dipole. (3.2)

The force applied to a dipole at $P_1$with magnetic moment m_1 by another dipole at P_2 with magnetic moment m_2 is approximated by

$$F_{12} \approx \frac{3\mu_o}{4\pi} \frac{1}{|p_2 - p_1|^4} \left[5n_{12}\big((m_1.n_{12})(m_2 n_{12})\big) - n_{12}(m_1.m_2) - m_1(m_2.n_{12}) - m_2(m_1.n_{12})\right]. \tag{3.3}$$

The torque applied on a dipole at p_2 by a dipole at p_1 is

$$\emptyset_{12} = m_2 \, \mathrm{X} \, B_{p_1}(p_2). \tag{3.4}$$

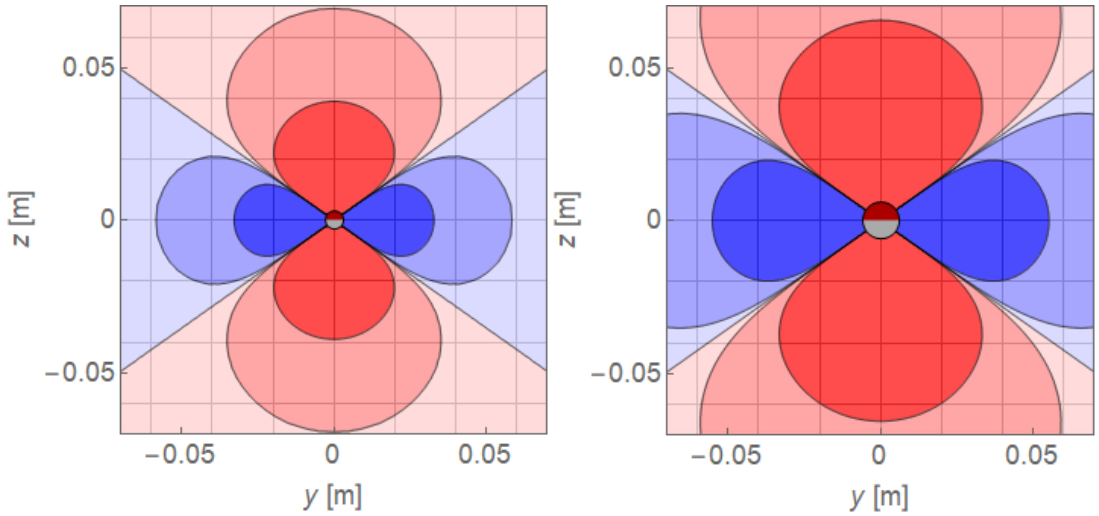

$\boldsymbol{r_{sphere}} = \mathbf{3}$mm $\qquad\qquad$ $\boldsymbol{r_{sphere}} = \mathbf{6mm}$

Figure 3.1 Contour lines show the force component radially outward from a sphere at (0,0) on an identical sphere in an MRI. The magnetic field is symmetric about the z-axis.

Inside a 3T MRI, a steel sphere becomes fully magnetized with magnetic saturation $M_s = 1.36 \cdot 10^6$.

The magnetic moment of a sphere with radius r_{sphere} is aligned with the MRI B_o field:

$$m\left(r_{\text{sphere}}\right) = \begin{bmatrix}0\\0\\1\end{bmatrix} \frac{4}{3}\pi r_{\text{sphere}}^3 M_s. \tag{3.5}$$

Figure 3.1 shows contour plots for the magnetic force exerted by two identical spheres on each other. The contour lines show $F \cdot n_{12}$, the force component radially outward from the sphere at (0,0) compared to the maximum force provided by the gradient coils gM . This force is attractive (red) along the z-axis and repulsive (blue) perpendicular to z-axis. The magnetic field is symmetric about the z-axis. If two spheres move within the dark red

region, they cannot be separated using the gradient field. The contour lines are drawn at $F_{12}.n_{12} = g_M.\left\{-1, -\frac{1}{10}, 0, \frac{1}{10}, 1\right\}$. The maximum force is along the z-axis is

$$F_{\text{attraction}} = -\frac{8M_s^2\mu_o\pi r_1^3 r_2^3}{3d^4}. \quad (3.6)$$

d: is the distance separating the two spheres with radii's r_1 and r_2.

M_s: is the magnetic saturation inside MRI = $1.36 \cdot 10^6$.

μ_o: vacuum permeability which is equal to $4\pi \cdot 10^{-7}$ V·s/(A·m).

3.2 Magnetic Torque on MRI Gauss Gun

Because each Gauss Gun component has two ferrous spheres, the MRI B_o field creates a torque that acts to line the components parallel to the *z*-axis. Applying (3.4), with magnetic moments given by (3.5), on a component with sphere radii's r_1 and r_2, separated by s, and the line between the spheres at an angle of θ from z, generates the restoring torque:

$$\tau = \frac{4}{3s^3} M_s^2 \pi \mu_o r_1^3 r_2^3 \sin(2\theta). \quad (3.7)$$

This torque increases by increasing r_1 and/or r_2 and decreasing s. This torque results in stable equilibrium configurations pointing along the $\pm z$-axis and unstable equilibriums perpendicular to the axis. The stable equilibriums correspond with maximum attractive force between the spheres, and the unstable equilibriums with maximum repulsive force. The average torque on the spheres is $\frac{4}{\pi}$ the average force between the spheres.

3.3 MRI Gauss Gun Design

This section shows the MRI Gauss Gun design and how it differs from the traditional Gauss Gun. MRI Gauss Gun contains three components: trigger component, barrel component and the delivery component, knowing that the number of stages N is the number stages in the barrel component and delivery component.

- Trigger component: This component is important to fire the Gauss Gun. Part (a) in Figure 3.2 represents the trigger component
- Barrel component(optional): is the middle stage(s) between the firing and delivery components, each stage has two spheres each sphere with radius r with a non-magnetic spacer s between the spheres, and between any two stages there is air gap a which greater than the spacer s, which necessary to the magnetized sphere to be released from own stage when firing. The barrel component used to achieve stronger forces. Part (b) in Figure 3.2 represents the barrel component. Figure 3.3 shows the case when there is no barrel component.
- Delivery component: one stage contains two spheres each sphere with radius r with a non-magnetic spacer s between the spheres, we can replace the delivery sphere to deliver a drug. While the delivery component used to administer the desired treatment or a drug delivery. Part (c) in Figure 3.2 represents the delivery component.

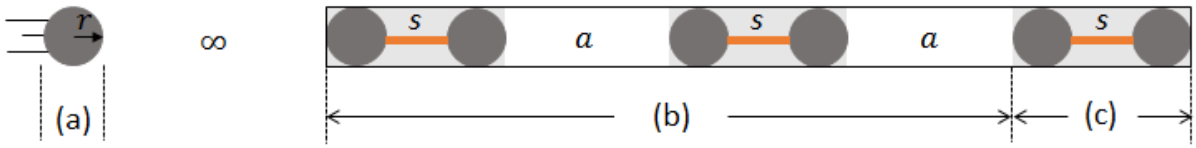

Figure 3.2 **Three stages MRI Gauss Gun with all the components, (a) Trigger component, (b) Barrel component contains two stages and (c) Delivery component.**

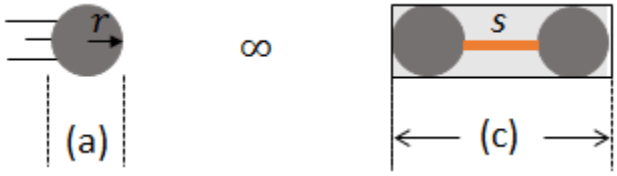

Figure 3.3 **One stage MRI Gauss Gun contains only of (a) Trigger component and (c) Delivery component with no barrel component.**

3.4 MRI Gauss Gun Materials

In this thesis the MRI Gauss Gun uses steel spheres (E52100 Alloy, McMaster 992K41) for the magnets and shaped rods of nonmagnetic metal for spacers s, which provides several benefits:

- Inside MRI, steel is a stronger magnet than neodymium
- Spacer length is arbitrary and can be chosen to maximize energy
- Leaving multiple magnets in tissue is potentially dangerous, leading, e.g., to bowel necrosis, perforation, volvulus, sepsis, and possible death [17][18]. In contrast, the steel bearing ball used in this thesis lose their magnetism when removed from the magnetic field.
- MRI enables imaging and control to assemble components at target.
- MRI enables controlled removal of components.

3.5 MRI Gauss Gun Magnetic Energy to Kinetic Energy

This section investigates how the energy system works in the MRI Gauss Gun. MRI Gauss Gun has *N* stages, each stage has two spheres each with radius *r* between them nonmagnetic spacer *s.* and between each two stages there is air gap *a.*

Before firing the system is stable, each stage has Potential Energy PE_{MB} and this energy needed to break the magnetic bond between them to release the millirobot from each stage. In 3.5.1 are the details for all kinetic and potential energies in MRI Gauss Gun system.

3.5.1 Kinetic and Potential Energies in MRI Gauss Gun System

This part of section 3.5 shows all the energies that form in MRI Gauss Gun. This section ignores the heat, fraction and any mechanical losses. This section also simplifies analysis by only considering forces between adjacent spheres since the nonadjacent spheres have small forces on each other which can be neglected.

- PE_{MB}: is the potential energy between any two millirobots inside each stage before firing, which is the same energy needed to break the magnetic bond between any two millirobots inside each stage. to find this energy we need to find the negative integration of $F_{attraction}$ in equation (3.6) which is:

$$PE_{\mathrm{MB}} = -\int_{d}^{\infty} -\frac{8M_s^2\mu_o\pi r_1^3 r_2^3}{3x^4}\,dx, \text{ then} \tag{3.8}$$

$$PE_{\mathrm{MB}} = \frac{C}{(2r+s)^3}. \tag{3.9}$$

- KE_{∞}: is the kinetic energy the fired sphere gains by the attraction force exerted while it approaches the first stage..

  We can find this kinetic energy using the following equations:

$$KE = -\Delta PE, \tag{3.10}$$

$$\Delta PE = -\int_{ref}^{r} F_{\text{attraction}}\, dx. \tag{3.11}$$

  Now from (3.6), (3.10) and (3.11) then

$$KE_{\infty} = \int_{\infty}^{2r} -\frac{8M_S^2\mu_o\pi r_1^3 r_2^3}{3x^4}\, dx. \tag{3.12}$$

  Assuming that the constant *C* includes all the terms except the distance between the spheres, and after doing the integration:

$$KE_{\infty} = \frac{C}{(2r)^3}. \tag{3.13}$$

- KE_a: is the kinetic energy the millirobot gains by the attraction force exerted on the sphere in the next stage when it moves a distance from the current stage to the next stage.

  Using equations (3.6), (3.10) and (3.11):

$$KE_a = \int_{a+2r}^{2r} -\frac{8M_S^2\mu_o\pi r_1^3 r_2^3}{3x^4}\, dx, \tag{3.14}$$

$$KE_a = \frac{8M_S^2\mu_o\pi r_1^3 r_2^3}{9(2r)^3} - \frac{8M_S^2\mu_o\pi r_1^3 r_2^3}{9(2r+a)^3} \text{ then} \tag{3.15}$$

$$KE_a = C\left[\frac{1}{(2r)^3} - \frac{1}{(2r+a)^3}\right]. \quad (3.16)$$

3.5.2 Numerical and Analytical Methods using Mathematica

In this part of section 3.5 is the energy system mechanism inside the MRI Gauss Gun and the derivation formula for the delivery component kinetic energy KE_f.

Before firing the barrel and delivery components are *stable* because there is a restoring force that would return any sphere to the stable position if a small displacement is applied. As shown in Figure 3.4 (a), each stage in these components has potential energy PE_{MB} and this energy needed to break the magnetic bond between them to release the millirobot from each stage. From there we can find that the system has energy losses equals to a number of stages times the potential energy. Equation (3.17) shows the energy losses in the system.

$$\text{Energy Losses} = N \cdot PE_{\text{MB}}. \quad (3.17)$$

After firing the trigger millirobot will hit the first millirobot in the first stage as in Figure 3.4(b) which represents the impact between the trigger component and the barrel component, in the impact step, KE_∞ transfer to the first stage, since KE_∞ is greater than PE_{MB}, that will break the magnetic bond in the first stage and will release the second ball from the first stage with energy equals to $KE_\infty - PE_{\text{MB}}$ as in Figure 3.4 (c).

Once sufficiently displaced from its stable resting position, the released sphere will propelled by attractive forces toward the first ball in the second stage. The released millirobot gains KE_a J of energy. The net energy gain will transfer to the next stage as in Figure 3.4 (d).

This process repeats until the sphere delivered to the last stage releases the delivery component, which will gain kinetic energy KE_f as in equation (3.18) which shows the final kinetic energy that the delivery component released with when the MRI Gauss Gun has N Stages.

$$KE_f = KE_\infty + (N-1)KE_a - (N)\,PE_{\mathrm{MB}}, \tag{3.18}$$

$$KE_f = \frac{C}{(2r)^3} + (N-1)\,C\left[\frac{1}{(2r)^3} - \frac{1}{(2r+a)^3}\right] - (N)\,\frac{C}{(2r+s)^3}, \text{ and} \tag{3.19}$$

$$KE_f = \frac{C}{(2r)^3}(N) - \left(\frac{C}{(2r+a)^3}\right)(N-1) - \frac{C}{(2r+s)^3}(N). \tag{3.20}$$

Note that when $N = 1$ which means no barrel component then the final kinetic energy equals to the following equation:

$$KE_f = \frac{C}{(2r)^3} - \frac{C}{(2r+s)^3}. \tag{3.21}$$

Figure 3.4 explains how the energy transfers inside three stages MRI Gauss Gun until it reaches the delivery part. You can apply the same idea to *N* stages MRI Gauss Gun.

KE_f for Figure 3.4 is:

$$KE_f = KE_\infty + 2KE_a - 3\,PE_{\mathrm{MB}} \text{ and} \tag{3.22}$$

$$KE_f = \frac{C}{(2r)^3}(N) - \left(\frac{C}{(2r+a)^3}\right)(N-1) - \frac{C}{(2r+s)^3}(N). \tag{3.23}$$

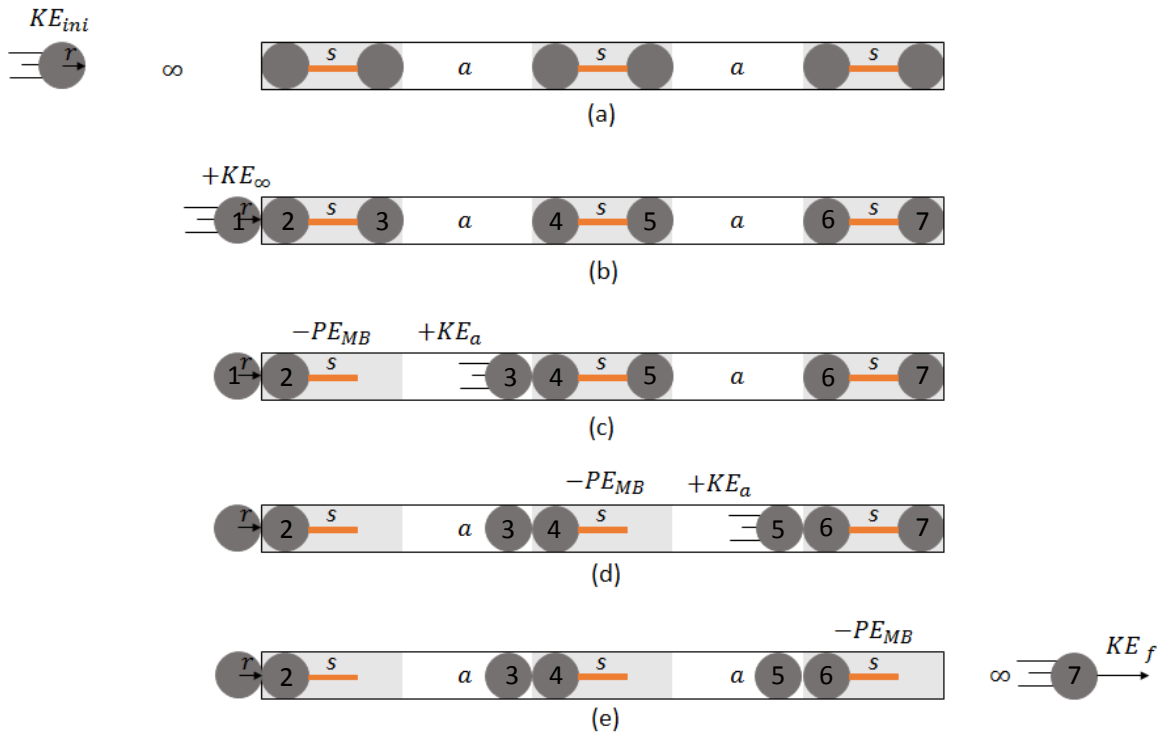

Figure 3.4 **Shows how the energy system works in three stage MRI Gauss Gun (a) The trigger component is moving with $+KE_\infty$_ini to the first stage from the MRI Gauss Gun, (b) Trigger component hits first sphere with energy equals to $+KE_\infty$, (c) Sphere 3 hits sphere 4 with energy equals to $+KE_\infty - PE_{MB} + KE_a$, (d) Sphere 5 hits sphere 6 with energy equals to $+KE_\infty - 2PE_{MB} + 2KE_a$and (e) The delivery part moves with energy $+KE_\infty - 3PE_{MB} + 2KE_a$.**

Chapter 4

MRI Gauss Gun Optimization – Analytical and Numerical Results

4.1 MRI Gauss Gun Restrictions

The medical procedure and dimensions of the human patient will provide several constraints on the size of the assembled Gauss gun and the length and radius of individual units. Assume we are given a constraint that the MRI Gauss Gun's total length must be less than or equal to L in which L includes all the components of the Gauss Gun as in Figure 4.1.

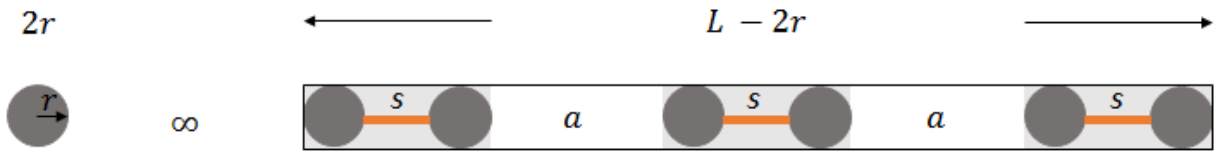

Figure 4.1 Three stage MRI Gauss Gun.

The following equation represents L as expressed in Figure 4.1:

$$L = 2(2N+1)r + Ns + (N-1)a. \quad (4.1)$$

This L is the first restriction, and the second restriction we have is that the air gap a between any two stages should be greater than the spacer s between any two spheres

inside each stage. The last restriction is a stability margin that prevents the MRI Gauss Gun from premature firing.

As shown in equation (4.1), for every N value L is a linear function of r, s and a. This property enables us to non-dimensionalize the optimization, allowing us to give design guidelines for any size of Gauss gunRecall equation (3.10) $KE = \frac{C}{(2r)^3}(N) - \left(\frac{C}{(2r+a)^3}\right)(N-1) - \frac{C}{(2r+s)^3}(N)$. (3.10)

The third restriction the design has is the millirobot radius, which we will discuss in Section 4.3, while Section 4.2 will analyze the optimization for the first and second restrictions only.

4.2 Analytical and Results

4.2.1 Numerical and Analytical Methods using Mathematica

Here, we are trying to maximize KE with the restriction L. As shown in equation (3.10), KE is a non-linear equation. To optimize KE we use *Mathematica* software which has four different numerical algorithms for constrained global optimization:

- **Differential Evolution:** is a simple stochastic function minimizer. The algorithm maintains a population of m points, $\{x_1, x_2, ..., x_m\}$, where typically $m>>n$, with n being the number of variables. This method is computationally expensive, but

relatively robust and tends to work well for problems that have more local minima [11].

- **Nelder Mead:** is a direct search method. For a function of *n* variables, the algorithm maintains a set of *n+1* points forming the vertices of a polytope in *n*-dimensional space. This method is often termed the "simplex" method, which should not be confused with the well-known simplex method for linear programming [11].
- **Random Search:** it works by generating a population of random starting points and uses a local optimization method from each of the starting points to converge to a local minimum. The best local minimum is chosen to be the solution [11].
- **Stimulated Annealing:** a simple stochastic function minimizer. It is motivated from the physical process of annealing, where a metal object is heated to a high temperature and allowed to cool slowly. The process allows the atomic structure of the metal to settle to a lower energy state, thus becoming a tougher metal. Using optimization terminology, annealing allows the structure to escape from a local minimum, and to explore and settle on a better, hopefully global, minimum [11].

In this optimization, we tried all four methods, and found the following:

Random search and Differential Evolution work for single point but they do not work when I use them in plot function, Stimulated Annealing and Nelder Mead optimization methods both work with plot function but the later method is much faster than Stimulated Annealing. For these reasons, we chose Nelder Mead in this optimization.

In our research the goal is to optimize KE in (3.10) using Nelder Mead Method for different N values for two cases:

Case 1: when all millirobots have the same radii, this is discussed in 4.2.2.

Case 2: when millirobots have different radii for $N = 1$ and $N = 2$, this case will be discussed in 4.2.3.

4.2.2 Numerical Analysis when all millirobots have the same radii

This part will show the optimization to find the optimum KE for the case when all millirobots have the same radii, Figure (4.1) shows the kineticEnergy[r,N] function created using Mathematica to find the optimum kinetic energy for the delivery millirobot given radius r and number of stages N.

```
kineticEnergy[r_, n_] := {

  crr = (8 Msat^2 π r^3 r^3 μ0 * 10^6)/9; (* crr is a constant includes all the terms except the distance between the spheres*)
  Msat = 1.36 × 10^6;
  μ0 = 4 π 10^-7;

  {ke, spacer, airgap} = With[{z = NMaximize[{crr (1/(2 * 10 r)^3) + crr (1/(2 * 10 r)^3 - 1/(a + 10 r)^3) * (n - 1) - crr * (1/(2 * 10 r + s)^3 * n)
      , s ≥ 0, a ≥ s, 10 (4 n + 2) r + n * s + (n - 1) a == 10}, {s, a}, Method → "NelderMead"]}, Extract[z, Position[z, _?NumericQ]]];

  ke / 10^3
 };
```

Figure 4.2 KineticEnergy[r,N] function created in Mathematica to be used in MRI Gauss Gun optimization.

The function in Figure 4.2 used to plot KE/L^3 Vs r/L for N from 1 to 10, KineticEnergy[r,N] function used to plot Figure 4.3 and also used to find the optimum value for each parameter as in Table 4.1.

Figure 4.3 represents the plot KE/L^3 Vs r/L for N from 1 to 10. In this plot, there are ten curves each curve represents the number of stages the MRI Gauss Gun has starting from one stage to ten stages, the red point on each curve represents the optimum KE value for each curve.

This plot has non-dimensionalized axes, you can use it for any L value, for instance, if KE/L^3 at r/L= 0.143 when N = 1 is 1664.6 J thus for L =10 mm, r will equal 1.43×10^{-2} and KE will equal 166.46×10^{-3}J. In section 4.4 we will show some study cases using Table 4.1 and Figure 4.3

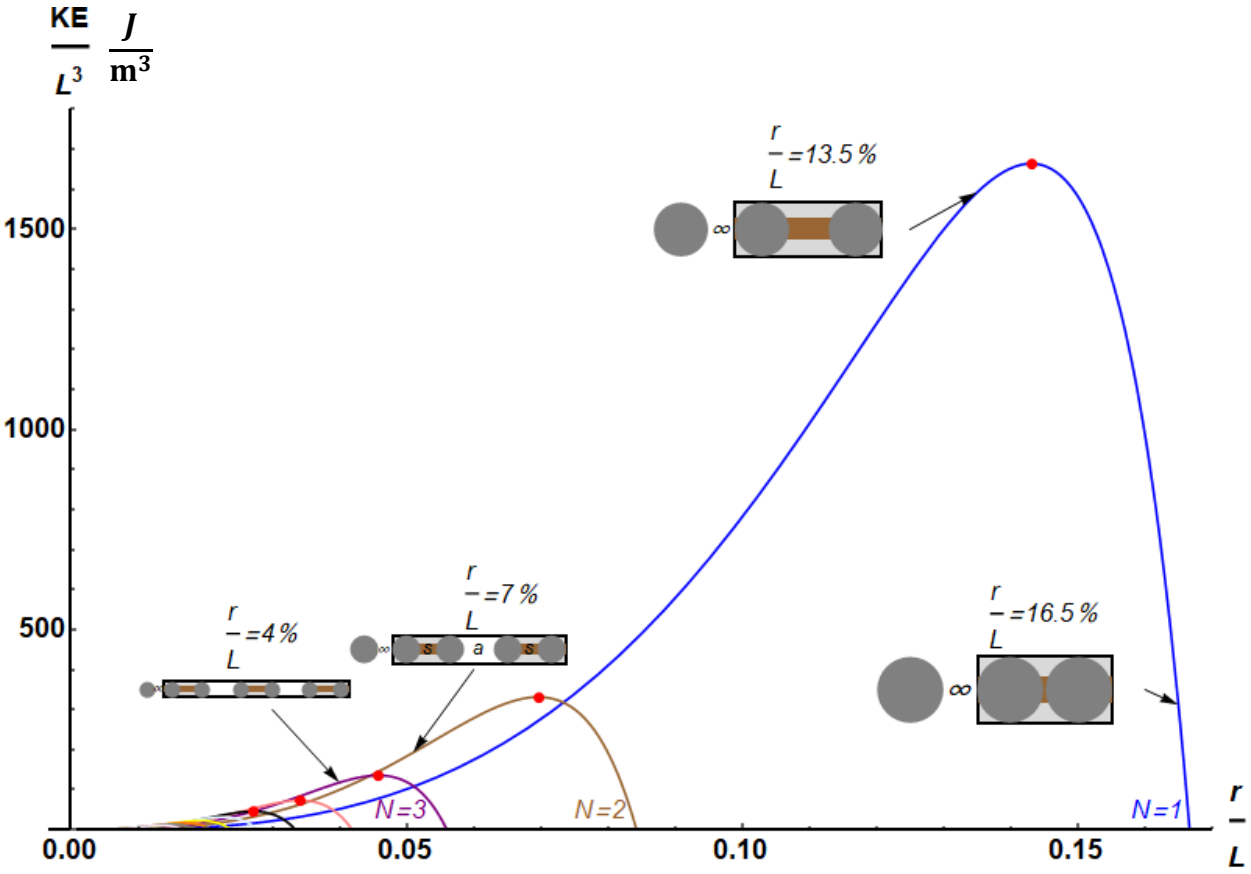

Figure 4.3 Plot KE/L^3 Vs r/L for N from 1 to 10. Each curve represents a stage. The red dots represent the optimum value for each stage.

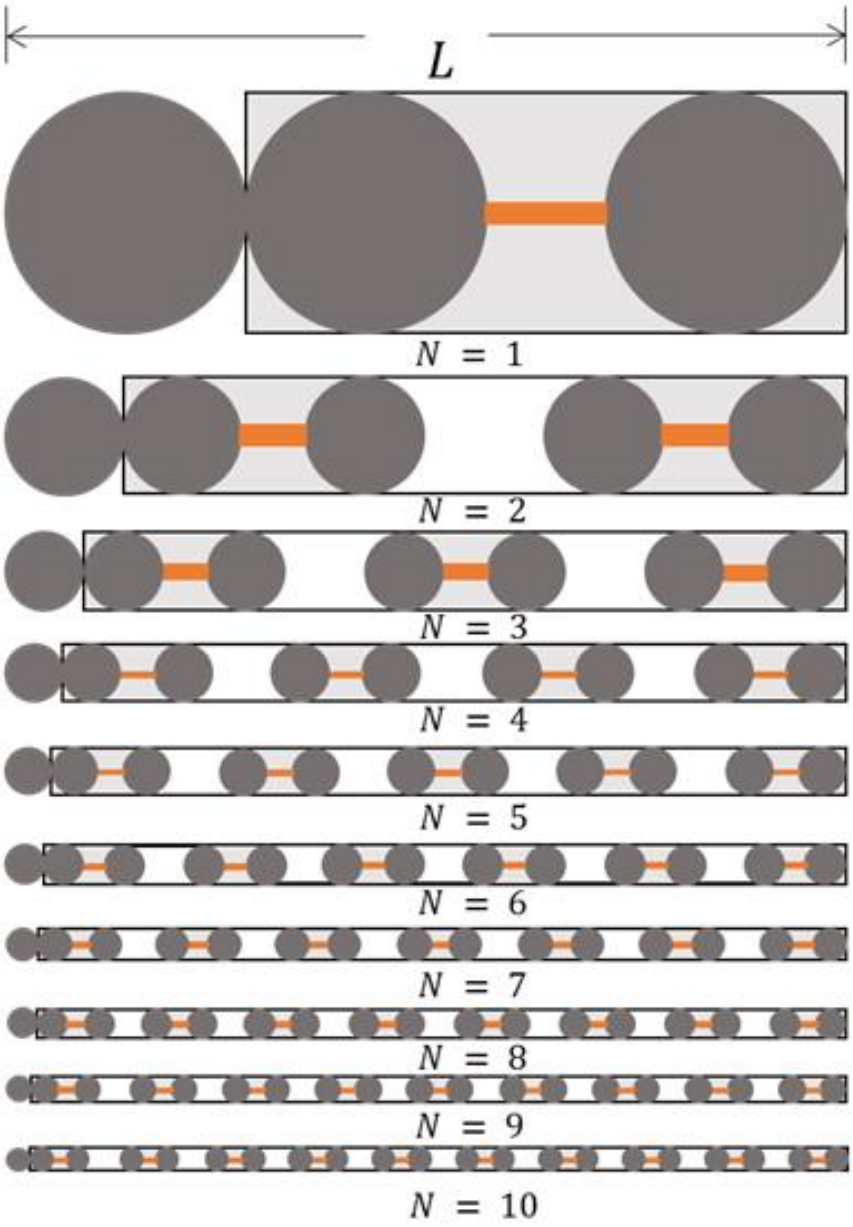

Figure 4.4 Different stage MRI Gauss Gun with the same length L

Table 4.1 Represents the optimum value in each stage from N = 1 to 10

n	r/L	s/L	a/L	KE/L^3
1	0.143	0.142	0	1664.6
2	0.07	0.078	0.148	331.5
3	0.046	0.053	0.099	135.7
4	0.034	0.041	0.074	73.2
5	0.027	0.032	0.06	45.6
6	0.023	0.027	0.0499	31.1
7	0.019	0.023	0.043	22.6
8	0.017	0.021	0.037	17.1
9	0.015	0.018	0.033	13.4
10	0.013	0.017	0.03	10.8

The next section describes optimization when MRI Gauss gun spheres have different radii.

4.2.3 Numerical Analysis using different radii when $N = 1$ and $N = 2$

4.2.1 showed the optimization for the situation when we have Length restriction with equal millirobot radii, in 4.2.2 we will show what will be the radii's values when we give the optimization the freedom to optimize for different r values when $N = 1$ and $N = 2$ using Nelder Mead method.

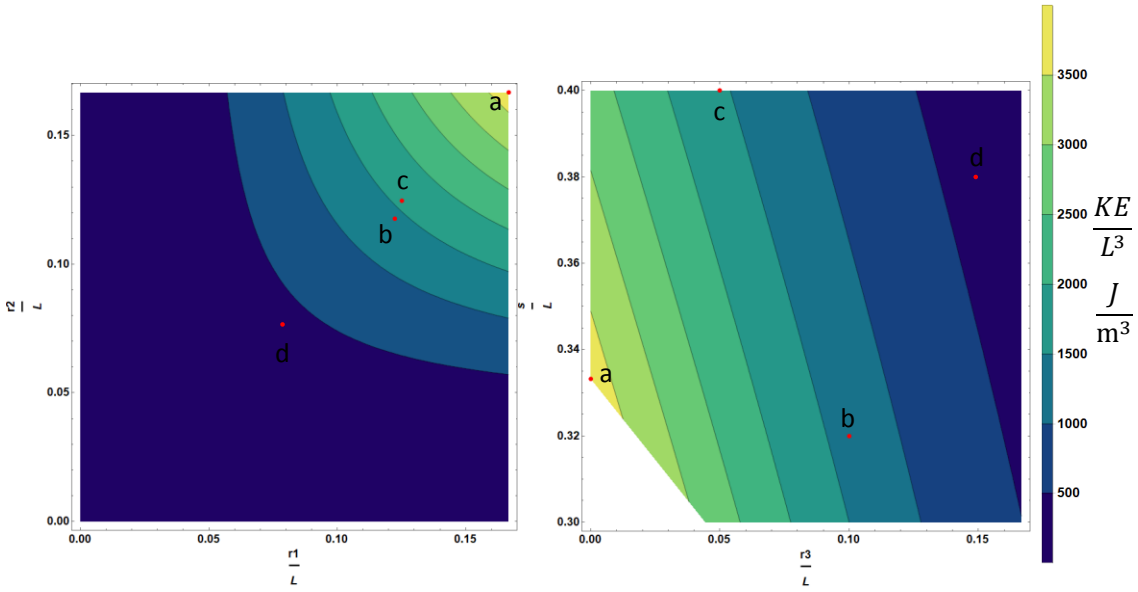

Figure 4.5 (a) Contour Plot for r_1/L Vs r_2/L, (b) Contour Plot for s/L Vs r_3/L.

Figure 4.5 shows the contour plots for one stage different radii case. While $\boldsymbol{r_1}$ is the fired ball radius, $\boldsymbol{r_2}$ is the second sphere radius and $\boldsymbol{r_3}$ is the third sphere radius and $\boldsymbol{s}$ is the spacer between the second and the third sphere. While figure 4.6 shows one stage MRI Gauss Gun for each red point on figure 4.5 and Table 4.2 shows the values for each red point.

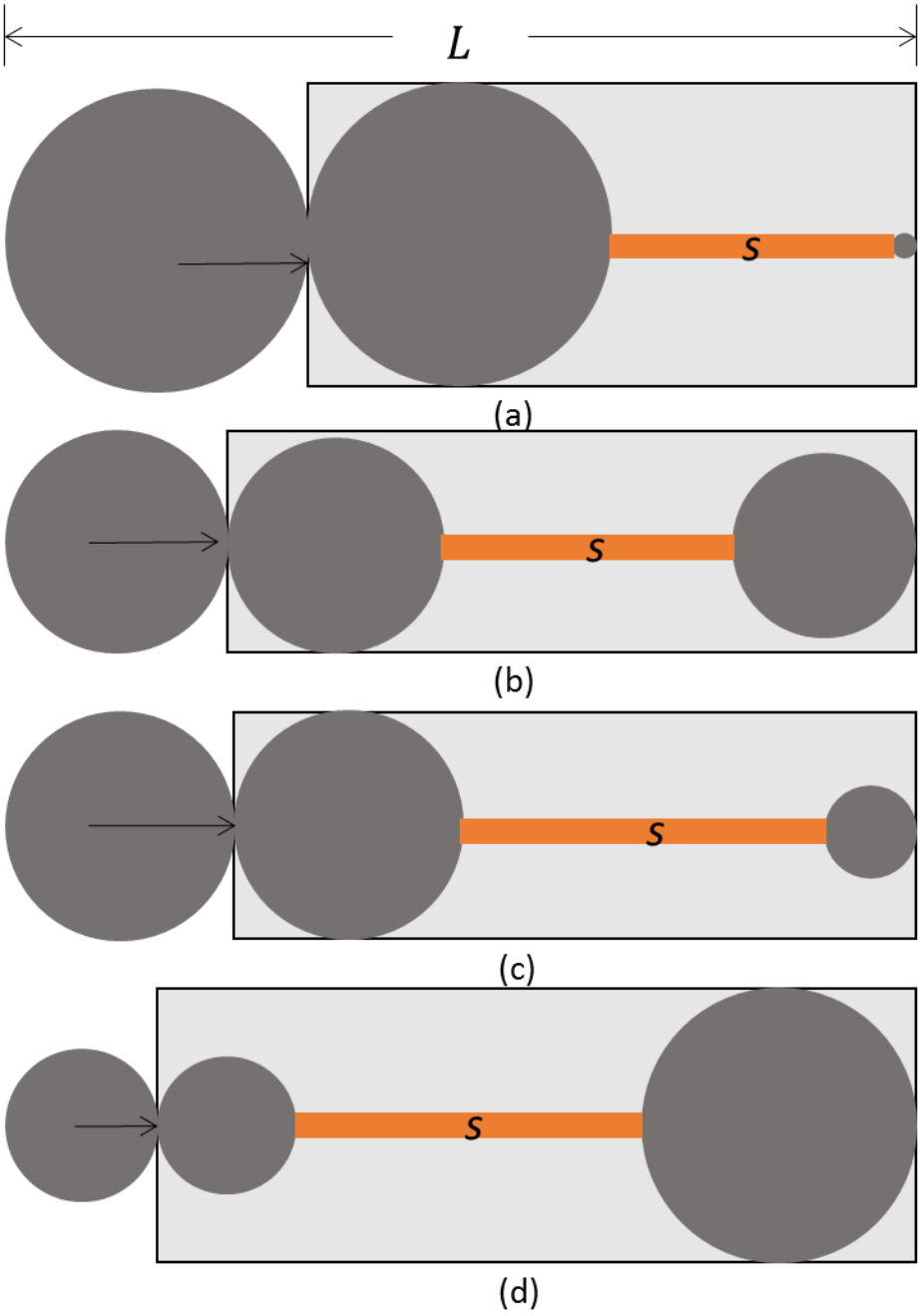

Figure 4.6 Shows different one stage MRI Gauss Gun that represent the red points in Figure 4.5.

Table 4.2 The optimal values for a single unit Gauss gun, shown as red points in Figure 4.4.

	$r1/L$	$r2/L$	$r3/L$	s/L	KE/L^3
A	0.167	0.167	0.0000666	0.3332	3756.14
B	0.122	0.118	0.1	0.32	1332.35
c	0.125	0.125	0.05	0.4	1576.3
d	0.084	0.076	0.15	0.38	369.085

From Figure 4.4 and Table 4.2 you can notice that the maximum KE occurred when the fired millirobots and the first millirobots radii maximized and the delivery part minimized with large spacer value. Optimization KE result from the different radii is greater than twice optimization KE result from the case when all radii are the same.

In Table 4.3 are the optimum values for $r, r1, r2, r3, r4, s, a$ and KE when $L = 1$, while r is the fired ball radius, *r1* is the first millirobot in the first stage radius, *r2* is the second millirobot in the first stage radius, *r3* is the first millirobot in the second stage radius, *r4* is the second millirobot in the second stage radius.

Table 4. 3 Shows the optimum values for r, r1, r2, r3, r4, s, a and KE when L=1.

N	r/L	$r1/L$	$r2/L$	$r3/L$	$r4/L$	s/L	a/L	KE/L^3
2	0.1	0.1	0.0785	0.1	≈ 0	0.066	0.112	1019.2

Table 4.3 shows that by not restricting the radii to be the same, KE = 1019.2 J which is about three times KE when there is a restriction to the radii to be the same.

Figure 4.7 shows the optimized two stage Gauss Gun.

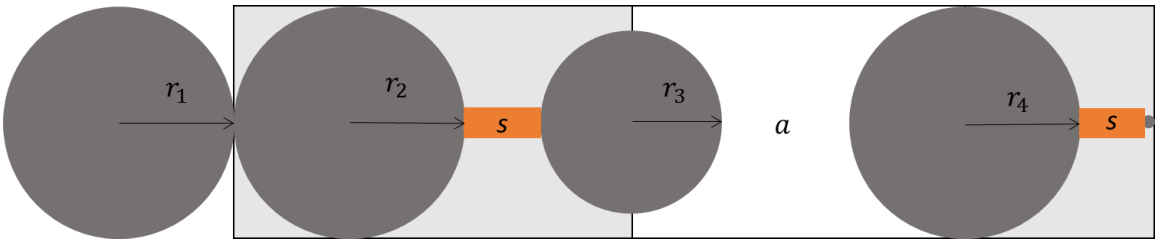

Figure 4.7 (a) One stage optimum MRI Gauss Gun with different radii case and (b) Two stages optimum MRI Gauss Gun with different radii case.

4.3 Study Cases

Using the results from section 4.2, in this section, we will use these results to apply them in real situations where we are using them to deliver the drug or remove clot from the body for different areas.

4.3.1 Study Case 1: Designing MRI Gauss Gun for brachytherapy delivery in the bladder (limited radius size to insert each component, very large area to assemble).

The bladder is a hollow muscular, and distensible (or elastic) organ that sits on the pelvic floor. Urine enters bladder via the ureters and exits via the urethra [25].

In this study case, the MRI Gauss Gun components will enter the bladder through the urethra for brachytherapy delivery for a tumor recovery. In this case, urethra radius

and the bladder length are the restrictions. The urethra diameter between 8 – 9 mm [26] and the bladder can be stretched from two inches to 6 inches [27] which is from 5 cm to 15 cm.

Here will use the average urethra radius 4.25 mm as the radius restriction, the average bladder length 10 cm as the MRI Gauss Gun length restriction and the last restriction is the brachytherapy seed radius which is 0.4 mm and that represents the delivery part in the MRI Gauss Gun.

Using Nelder Mead method in Mathematica software we got the optimum values $a, s\ and\ N$ as the code in Figure 4.9. which gives $a = 26.6$ mm $, s = 17.5$ mm $and\ N = 2$ to get KE = 12.1 mJ.

```
Clear[a, s, n, r]
r = 4.25 * 10^-3;
rbrachy = 4.5 * 10^-3;

NMaximize[{8 Msat^2 π r^3 r^3 μ0/9 (1/(2 * r)^3) + 8 Msat^2 π r^3 r^3 μ0/9 (1/(2 * r)^3 - 1/(a + r)^3) * (n - 1) - 8 Msat^2 π r^3 r^3 μ0/9 * (1/(2 * r + s)^3) * (n),
  s ≥ 0, 2 (2 n) r + n * s + (n - 1) a + rbrachy ≤ 10 * 10^-2}, {s, a, n}, Method → "NelderMead"]
```

Figure 4.8 Mathematica code to find the optimum value for a,s and N to optimize KE inside the bladder

Figure 4.9 shows the Optimized MRI Gauss Gun to fit inside the bladder and figure 4.10 shows the MRI Gauss Gun inside the bladder.

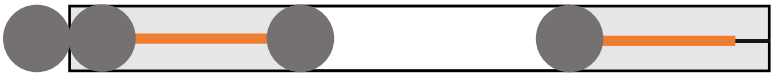

Figure 4.9 Optimized MRI Gauss Gun to fit inside the bladder

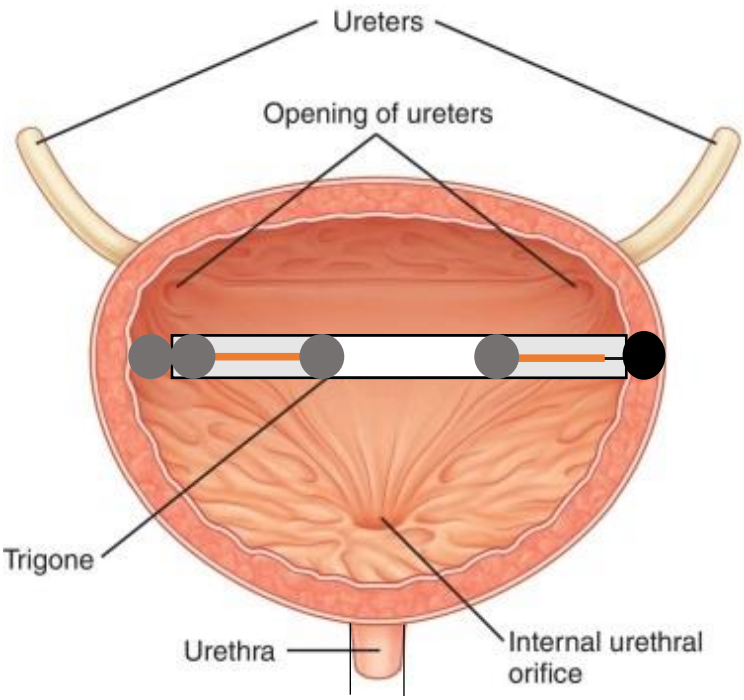

Figure 4.10 Schematic showing an MRI Gauss Gun inside a bladder

4.3.2 Study Case 2: Designing MRI Gauss Gun for *cyst fenestration* in brain ventricle, entry through the spinal canal.

This study case will show how to use the MRI Gauss Gun to deliver a drug to the brain ventricle by entering through the spinal canal. Knowing that a millirobot designed to fit through a 2.5 mm channel could navigate the side or posterior subarachnoid spaces in about 50% of the population, while the device that designed to fit through 1.5 mm channel would fit in more than 85% of the population. Gaining access to the ventricles of the brain from the spine is accomplished by passing through the cerebral aqueduct [31].

From another study, they found that the length for the lateral ventricle's size depends on the age and gender as the following Table4.4 [28].

Table 4.4 CT scan measurements (mean ±standard deviation) of frontal horn of lateral ventricle. https://www.researchgate.net/publication/268449358_Age-related_changes_in_ventricular_system_of_brain_in_normal_individuals_by_computed_tomography_scans

Age	Length (mm) for Males	Length (mm) for females
15 – 30	28.05 ± 2.1	27.6 ± 1.7
31 – 50	31.7 ± 2.3	28.0 ± 1.7
51 – 70	32.5 ± 2.3	30.05 ± 2.0

Here will use the millirobot radius to be 0.75 mm for each component as a radius restriction to fit more than 85% of the population, for lateral ventricles this study will show the MRI Gauss Gun for two situations male and female in the age range 31 – 50 as in Table 4.4 as the MRI Gauss Gun length restriction and the last restriction is the brachytherapy seed radius which is 0.4 mm and that represents the delivery part in the MRI Gauss Gun.

4.3.2.a: Case 1 Length restriction using male lateral ventricle length

This case uses L = 31.7 mm, r = 0.75 mm, delivery millirobot radius = 0.4 mm and length 4.5 mm. Using Nelder Mead method in Mathematica software we got the optimum values $a, s \; and \; N$ as the code in Figure 4.11. Nelder Mead method gives $a =$ 2.7 mm $, s = 1.8$ mm $\; and \; N = 4$ to get KE = 1.18 mJ.

```
Clear[a, s, n, r]
r = 0.75 * 10^-3;
rbrachy = 4.5 * 10^-3;

NMaximize[{(8 Msat^2 π r^3 r^3 μ0)/9 (1/(2*r)^3) + (8 Msat^2 π r^3 r^3 μ0)/9 (1/(2*r)^3 - 1/(a+r)^3) * (n-1) - (8 Msat^2 π r^3 r^3 μ0)/9 * (1/(2*r+s)^3) * (n),
  s ≥ 0, 2 (2 n) r + n*s + (n-1) a + rbrachy ≤ 31.7*10^-3}, {s, a, n}, Method → "NelderMead"]
```

Figure 4.11 Mathematica code to find the optimum value for a,s and N to optimize KE inside male brain ventricle

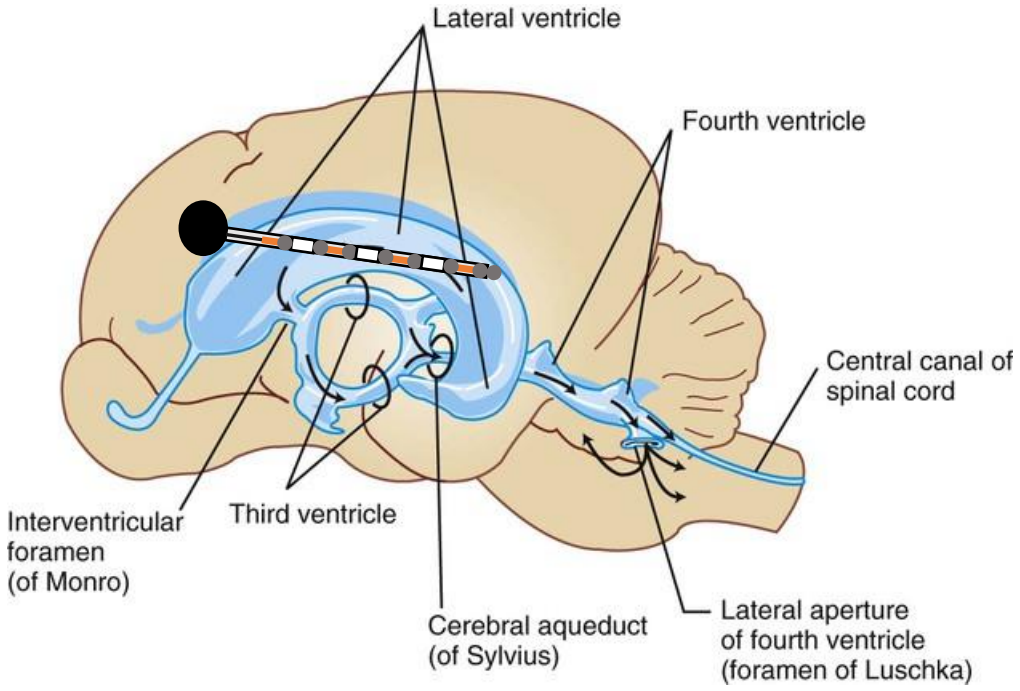

Figure 4.12 Schematic showing an MRI Gauss Gun inside male brain ventricle

4.3.2.b: Case 2 Length restriction using female lateral ventricle length

This case uses L = 28 mm, r = 0.75 mm, delivery millirobot radius = 0.4 mm and length 4.5 mm. Using Nelder Mead method in Mathematica software we got the optimum values $a, s \; and \; N$ as the code in Figure 4.13. which gives $a = 3.54$ mm $, s = 2.48$ mm $\; and \; N = 3$ to get KE = 1 mJ.

```
Clear[a, s, n, r]
r = 0.75 * 10^-3;
rbrachy = 4.5 * 10^-3;

NMaximize[{(8 Msat^2 π r^3 r^3 μ0)/9 (1/(2 * r)^3) + (8 Msat^2 π r^3 r^3 μ0)/9 (1/(2 * r)^3 - 1/(a + r)^3) * (n - 1) - (8 Msat^2 π r^3 r^3 μ0)/9 * (1/(2 * r + s)^3) * (n),
  s ≥ 0, 2 (2 n) r + n * s + (n - 1) a + rbrachy ≤ 28 * 10^-3}, {s, a, n}, Method → "NelderMead"]
```

Figure 4.13 Mathematica code to find the optimum value for a,s and N to optimize KE inside female brain ventricle

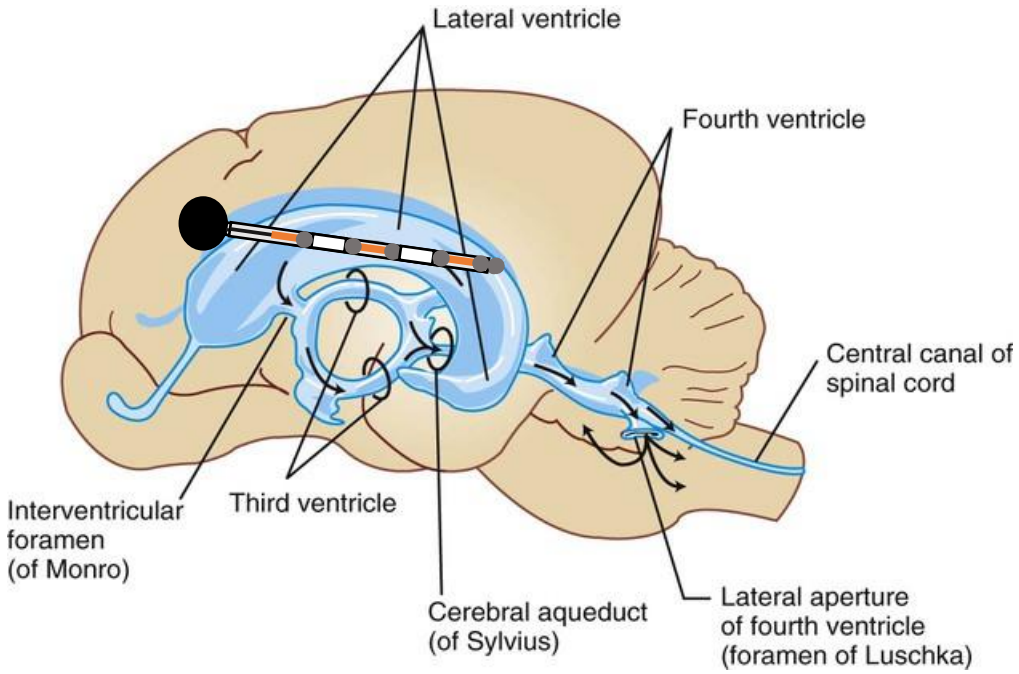

Figure 4.14 Schematic showing an MRI Gauss Gun inside female brain ventricle

4.3.3 Study Case 3: Designing MRI Gauss Gun for clot removal case from the coronary artery.

In this study case we will show the design for the MRI Gauss Gun to remove the clot from the coronary artery.

To remove a clot from coronary artery we need to let the MRI Gauss Gun components enter the body from an artery from the groin area Figure 4.11 in the leg then navigate them through the Aorta to the left coronary artery Figure 1.4. Knowing that Aorta and the arteries from the groin area are bigger diameters bigger than the coronary which has the smallest diameter between them with 4.6 mm, because of that we will use it as radius restriction, with 1.9 cm length which will be used as L restriction [29].

In this study case we will use the radius 2.3 mm as radius restriction and $L =$ 1.9 cm as Length restriction, using Nelder Mead method to optimize s, a and N to get the optimum KE.

Using the code in Figure 4.10, we will get the following results:

$s = 2.1$ cm, $a = 0$ and $N = 1$.

```
r = 2.3 * 10^-3;

NMaximize[{8 Msat^2 π r^3 r^3 μ0/9 (1/(2*r)^3) + 8 Msat^2 π r^3 r^3 μ0/9 (1/(2*r)^3 - 1/(a+r)^3) * (n-1) - 8 Msat^2 π r^3 r^3 μ0/9 * (1/(2*r+s)^3) * (n),
  s ≥ 0, 2 (2 n + 1) r + n * s + (n - 1) a ≤ 1.9 * 10^-2}, {s, a, n}, Method → "NelderMead"]
```

Figure 4.15 Mathematica code to find the optimum value for a, s and N to optimize KE.

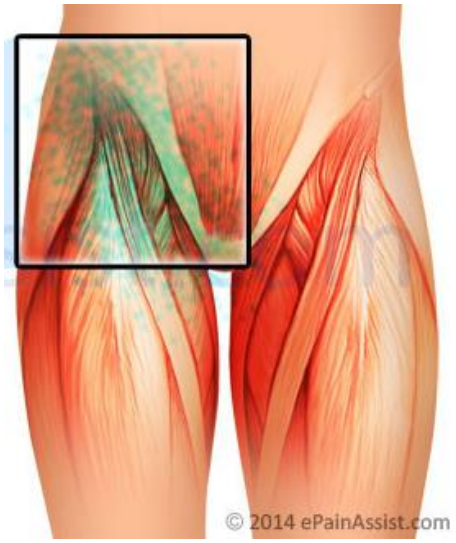

Figure 4.16 Groin area. Image credit: https://www.epainassist.com/pelvic-pain/groin-pain.

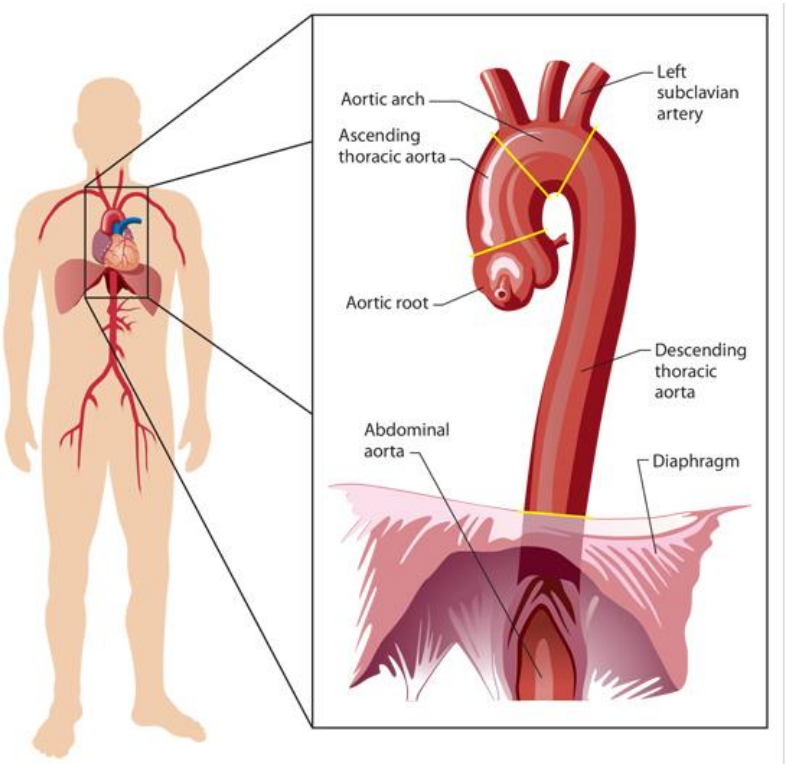

Figure 4.17 Aorta Anatomy. Image credit: http://www.jems.com/articles/print/volume-41/issue-3/features/how-aortic-aneurysms-become-aortic-catastrophes.html.

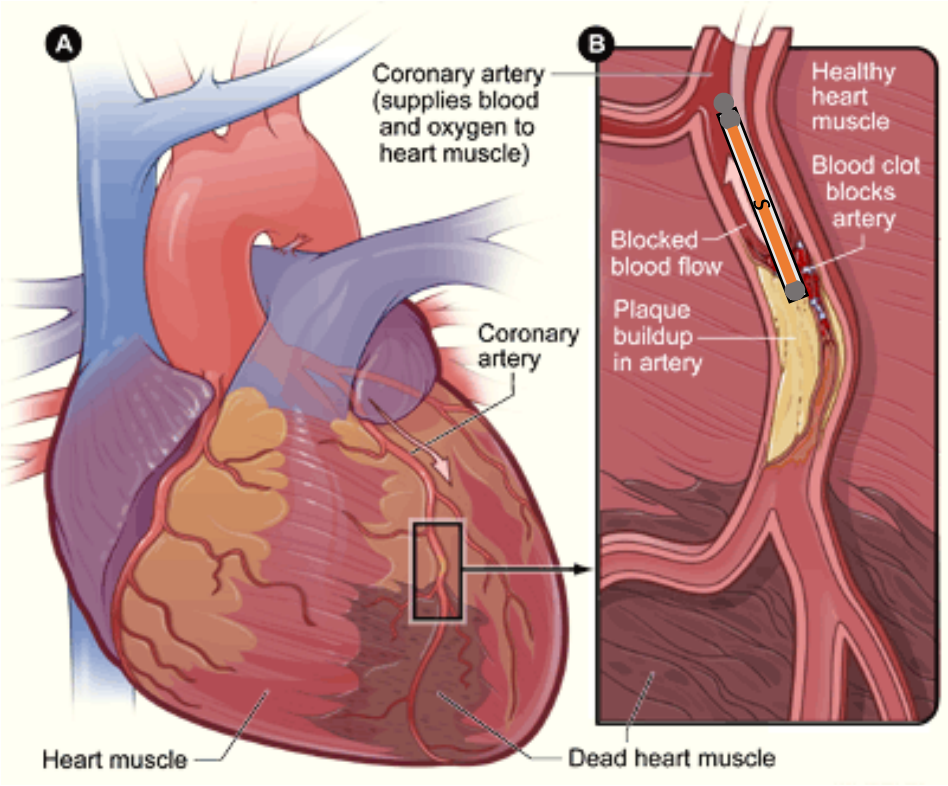

Figure 4.18 Schematic showing an MRI Gauss Gun inside coronary artery

Note: using MRI Gauss Gun is not recommended because of the blood flow and in the arteries.

Chapter 5

Conclusion

This thesis presented a model, optimization, and applications for MRI Gauss Gun. The traditional Gauss Gun depends on permanent magnets and steel spheres, while The MRI Gauss Gun can be self-assembled into a larger tool to increase final kinetic energy for the delivery component. The Analysis performed using Nelder Mead method build-in function in Mathematica software to optimize the MRI Gauss Gun with length restriction. Also, this thesis shows potential applications for the MRI Gauss Gun.

Future work can be in the following three categories:

- Design
    - Miniaturization (and why)
    - Bio-compatibility
    - Neurtral buoyancy
- Procedure
    - Disassembly
    - Recovery of components
    - Insertion
- Testing
    - Animal tests
    - Partnership with doctors

- Phantom test MRI

References

[1] Igor Paprotny and Sarah Bergbreiter Book: "Small Scale Robotics From Nano to Millimeter Sized Robotics and Applications"

[2] R. C. Ritter, M. S. Grady, M. A. H. III, and G. T. Gillies, *"Computer-integrated Surgery: Technology and Clinical Applications"*. The MIT Press, 1996, ch. 26 Magnetic Stereotaxis: Computer-Assited, Image-Guided Remote Movement of Implants in the Brain, pp. 363–370.

[3] K. Ishiyama, M. Sendoh, A. Yamazaki, and K. Arai, *"Swimming micro-machine driven by magnetic torque,"* Sensors and Actuators A: Physical, vol. 91, no. 1, pp. 141–144, 2001.

[4] A. Chanu, O. Felfoul, G. Beaudoin, and S. Martel, *"Adapting the clinical MRI software environment for real-time navigation of an endovascular untethered ferromagnetic bead for future endovascular interventions,"* Magn Reson Med, vol. 59, no. 6, pp. 1287–1297, Jun. 2008.

[5] P. Vartholomeos, M. Akhavan-Sharif, and P. E. Dupont, *"Motion planning for multiple millimeter-scale magnetic capsules in a fluid environment,"* in IEEE Int. Conf. Rob. Aut., May 2012, pp. 1927–1932.

[6] P. Vartholomeos, C. Bergeles, L. Qin, and P. E. Dupont, *"An MRI-powered and controlled actuator technology for tetherless robotic interventions,"* Int. J. Rob. Res., vol. 32, no. 13, pp. 1536–1552, 2013.

[7] A. Becker, O. Felfoul, and P. E. Dupont, *"Simultaneously powering and controlling many actuators with a clinical MRI scanner,"* in IEEE/RJS International Conference on Intelligent Robots and Systems (IROS), 2014, pp. 2017–2023.

[8] A. Eqtami, O. Felfoul, and P. E. D. E. Dupont, *"MRI-powered closed-loop control for multiple magnetic capsules,"* in IEEE/RSJ Int. Conf. Intelligent Robots and Systems, 2014, pp. 3536–354.

[9] A. Bigot, C. Tremblay, G. Soulez, and S. Martel, *"Magnetic resonance navigation of a bead inside a three-bifurcation pmma phantom using an imaging gradient coil insert,"* Robotics, IEEE Transactions on, vol. 30, no. 3, pp. 719–727, June 2014.

[10] W. K. Cho, J. A. Ankrum, D. Guo, S. A. Chester, S. Y. Yang, A. Kashyap, G. A. Campbell, R. J. Wood, R. K. Rijal, R. Karnik, R. Langer, and J. M. Karp, *"Microstructured barbs on the north american porcupine quill enable easy tissue penetration and difficult removal,"* Proceedings of the National Academy of Sciences, vol. 109, no. 52, pp. 21 289–21 294, 2012. [Online]. Available: http://www.pnas.org/content/109/52/21289.abstract

[11] O. Felfoul, A. Becker, C. Bergeles, and P. E. Dupont, *"Achieving commutation control of an MRI-powered robot actuator,"* IEEE Trans. on Robotics, vol. under review, 2014.

[12] M. Mahvash and P. Dupont, *"Mechanics of dynamic needle insertion into a biological material,"* Biomedical Engineering, IEEE Transac-tions on, vol. 57, no. 4, pp. 934–943, April 2010.

[13] J. A. Rabchuk, *"The gauss rifle and magnetic energy,"* The Physics Teacher, vol. 41, no. 3, pp. 158–161, 2003.

[14] D. Kagan, *"Energy and momentum in the gauss accelerator,"* The Physics Teacher, vol. 42, no. 1, pp. 24–26, 2004.

[15] R. Schill, *"General relation for the vector magnetic field of a circular current loop: a closer look,"* Magnetics, IEEE Transactions on, vol. 39, no. 2, pp. 961–967, Mar 2003.

[16] A. T. Becker, *"Optimizing a Gauss Gun, Wolfram Demonstrations Project,"* Oct. 2014. [Online]. Available: http://demonstrations. wolfram.com/OptimizingAGaussGun/

[17] C. for Disease Control, Prevention, *"Gastrointestinal injuries from magnet ingestion in children–united states, 2003-2006,"* MMWR: Morbidity and Mortality Weekly Report, vol. 55, no. 48, pp. 1296–1300, 2006.

[18] M. F. Kircher, S. Milla, and M. J. Callahan, "Ingestion of magnetic foreign bodies causing multiple bowel perforations," Pediatric radiol-ogy, vol. 37, no. 9, pp. 933–936, 2007.

[19] I. Howard, M.A, B. Abkes, M. Ollendieck, M. Noh, R. C. Ritter, and

G. Gillies, *"Measurement of the force required to move a neurosurgical probe through in vivo human brain tissue,"* Biomedical Engineering, IEEE Transactions on, vol. 46, no. 7, pp. 891–894, July 1999.

[20] O. Felfoul, J.-B. Mathieu, G. Beaudoin, and S. Martel, *"In vivo mr-tracking based on magnetic signature selective excitation,"* Medical Imaging, IEEE Transactions on, vol. 27, no. 1, pp. 28–35, 2008.

[21]http://reference.wolfram.com/language/tutorial/ConstrainedOptimizationGlobalNumerical.html

[22] Arsène Chemin, , Pauline Besserve, , Aude Caussarieu, , Nicolas Taberlet, and Nicolas Plihon *"Magnetic cannon: The physics of the Gauss rifle."*

[23] John Walker-Smith, Simon Murch, Linda Cardozo, *"Diseases of the Small Intestine in Childhood"* , CRC Press p.16

[24] Igor Paprotny and Sarah Bergbreiter *"Small-Scale Robotics from Nano-to-Millimeter-Sized Robotic Systems and Applications,"* first international workshop at ICRA 2013, Karlsrihe, Germany, May 6, 2013, Revised and Extended Papers

[25] Boron, Walter F, Boulpaepm Emile L. *"Medical Physiology,"* Elsevier Health Sciences. P. 738. ISBN 9781455733286.

[26] J.Talati, *" URETHRAL DILATATION,"* department of surgery, Aga Khan University of Health Sciences, Karachi.

[27] Healthline medical team, "In depth Bladder", March 10,2015

[28] Bijayalakhmi Parija, Shakti Rath, Niranjan Sahu and Rabindra N Padhy, *"Age – related changes in ventricular system of brain in normal individuals by computed tomograohy scans,"* November 2014

[29] Pamela S.Douglas, John Fiiolkoski, Barbara Berko and Nathaniel Reichek, *" Echocardiographic visualization of coronary artery anatomy in the adult,"* Journal of the American College of Cardiology.

[30] Katie Thomas, " Brothers Develop New Device to Halt Allergy Attacks", New York Times, 2013

[31] Bradley J. Nelson, Ioannis K. Kaliakatos and Jake J. Abbott, *"Microrobots for Minimally Invasive Medicine."*

[32] Aaron T. Becker, Member, IEEE, Ouajdi Felfoul, and Pierre E. Dupont, Fellow, IEEE *, "Toward Tissue Penetration by MRI-powered Millirobots Using a Self-Assembled Gauss Gun paper."*

[34] http://www.efunda.com/designstandards/springs/calc_comp_designer.cfm.